LANGMUIR

pubs.acs.org/Langmuir Article

Chromatographic Effects in Inkjet Printing

Gianmarco Venditti, Vignesh Murali, and Anton A. Darhuber*

Cite This: *Langmuir* 2021, 37, 11726–11736 Read Online

ACCESS | Metrics & More | Article Recommendations

ABSTRACT: We have studied the chromatographic separation of solvents and dyes after deposition of a dye solution on a paper substrate. Due to their larger molecular size, dyes typically exhibit a stronger interaction with the paper constituents. Consequently, the imbibition process of the dye is usually delayed compared to that of the solvent. This impacts the achievable resolution and color homogeneity in inkjet printing. We present experiments and a comprehensive numerical model to illustrate and quantify these effects. The model accounts for the solvent evaporation, heat transfer, multicomponent unsaturated flow, and dye adsorption, as well as the presence of permeable fibers in the paper substrate. We identify the key parameters that can be tuned to optimize the pattern fidelity of the printing process.

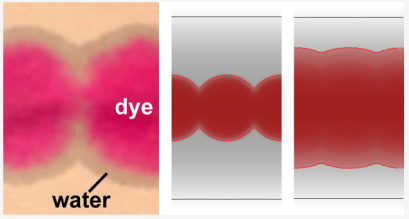

INTRODUCTION

Chromatography is an analytical technique employed for the separation of a multicomponent liquid or gaseous sample during flow through a polymeric or porous matrix based on the different molecular interactions of the individual components with the host matrix.[1] The individual components move at smaller average speeds than the solvent and accumulate into bands or peaks. The shape of the peaks and the speed of propagation contain information on specific interactions. In thin-layer chromatography, paper substrates are frequently used.[2,3] In the corresponding paper-based microfluidic devices, the flow mechanism is usually based on spontaneous capillary imbibition.[4,5]

Printing inks are typically multicomponent solutions of colorants, surfactants, humectants, and numerous other additives in aqueous or organic solvents.[6] Upon contact with paper, capillary imbibition causes the flow of the solution. While progressive absorption of the solvent into the paper is usually desirable, it is generally undesirable if the ink colorants are transported significant distances from the ink deposition zone, as this diminishes the achievable resolution of the printing process. Similarly undesirable is the chromatographic separation of dye mixtures or non-homogeneous dye concentration profiles because these degrade the color uniformity and contribute to edge mottling.

Donigian *et al.* studied the chromatographic retention of dyes on thin coating layers frequently used as top coats on high-quality paper types optimized for inkjet printing.[7] They studied the effect of the binder concentration on coatings containing either silica or calcium carbonate nanoparticles. Sodhi *et al.* and Filenkova *et al.* applied secondary ion mass spectrometry to characterize the spatial distributions of various ink components after inkjet printing of a long line with an approximate width of 200 μm.[8,9] For a coated paper, the line width is homogeneous, whereas for an uncoated paper, the line edges are ragged. In both cases, however, the dye front clearly lags behind the ink vehicle front.

Lamminmäki *et al.* studied the chromatographic separation of an anionic dye in thin porous layers composed of porous $CaCO_3$ microparticles and either anionic or cationic binders.[10] These materials are commonly used as coating top layers in photo-quality papers optimized for inkjet printing. The porous layer was oriented vertically and dipped into a horizontal reservoir filled with an aqueous solution of an anionic dye. Depending on whether the charges of the dye and the host matrix were of equal or opposite polarity, the retention of the dye molecules was either weak or very strong during the propagation of the water front up the porous layer.

The purpose of this paper is to present a numerical model for the imbibition and evaporation of a dye-based model ink containing a molecularly dissolved colorant in a solvent into and from paper substrates. The presence of fibers in the paper substrate is explicitly taken into account. The dye–paper interaction is described by the Langmuir-type rate equation for adsorption and desorption. The numerical simulations are complemented by experiments using anionic and cationic fluorescent dyes deposited either by drop-casting or inkjet printing.

MATERIALS AND METHODS

The paper type we used was Mondi DNS HSI NF with a thickness t_p = 104 μm, which contains $CaCl_2$ to aid the inkjet print quality. We used two different fluorescent dyes: the cationic red dye Rhodamine B

Received: June 17, 2021
Revised: September 10, 2021
Published: September 29, 2021

https://doi.org/10.1021/acs.langmuir.1c01624
Langmuir 2021, 37, 11726–11736

(Sigma-Aldrich; product number: R6626; molecular weight (MW): 479.02) and the anionic green dye fluorescein sodium salt (FSS; Sigma-Aldrich, product number: 46960, MW: 376.27). Solutions of various initial concentrations c_0 were prepared with demineralized water.

For our experiments, we used two different deposition methods: drop casting using a digital syringe (Hamilton, product number: 80065, capacity: 10 μL) and inkjet deposition using a droplet-on-demand printhead (Microdrop, model MDK-140-020). The corresponding experimental setups are sketched in Figure 1a,c. In both cases, the paper substrates are mounted about 6 mm above a solid surface, that is, both sides of the paper are surrounded by air rather than being in contact with a solid surface. In the inkjet setup, the paper is mounted on a motorized translation stage, which allows moving the paper substrate laterally with a speed U_{IJ} ranging from 0.05 to 5 mm/s. The inkjet setup and the corresponding experimental procedures are described in detail in ref 11. In the drop-casting experiments, a droplet of approximate volume of 5 μL was first formed at the nozzle of a syringe. Subsequently, the syringe was lowered using a lab jack (Thorlabs, product number: L490) until the drop made contact with the horizontal paper substrate. The syringe was maintained in this position for the entire duration of the experiment. Since it was not oriented exactly vertically, the drop footprint shape deviated from an exact circle, which explains the slightly oblong proportions of the water and dye fronts in Figure 1d.

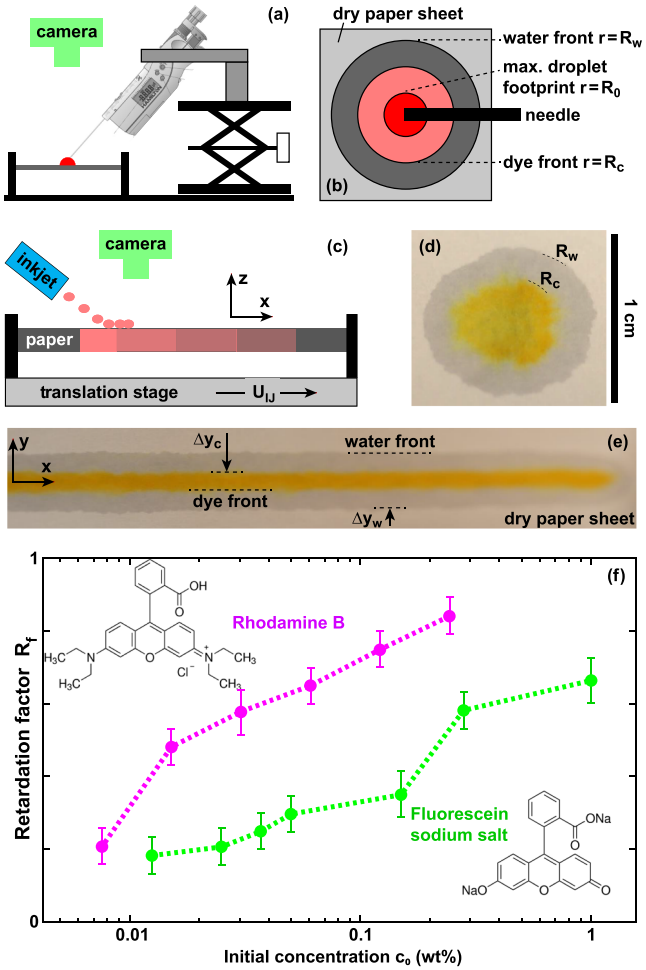

Figure 1. (a) Sketch of the drop-casting setup. (b) Definitions of relevant positions. (c) Sketch of the inkjet deposition setup. (d,e) Top view photographs after (d) drop casting an FSS solution (c_0 = 0.025 wt %) and (e) inkjet printing an FSS line (c_0 = 0.05 wt %; U_{IJ} = 0.5 mm/s). The water and dye fronts are indicated. The scale bar in (d) applies also to (e). (f) Retardation factor R_f for Rhodamine B and FSS solutions on a Mondi DNS HSI NF paper as a function of initial concentration c_0 extracted from drop-casting experiments. The insets illustrate the molecular structures of the dyes.

Figure 1d,e presents typical results of the drop-casting and inkjet deposition experiments using FSS solutions. It is clearly visible that the dye front fell behind the water front. For drop-casting experiments, we quantify this separation of the water and dye fronts by means of the retardation factor R_f defined as the ratio of the maximum propagation distances of the dye front and the water front

$$R_f \equiv \frac{\max(R_c) - R_0}{\max(R_w) - R_0} \tag{1}$$

Here, R_c, R_w, and R_0 are the positions of the colorant front, the water front, and the footprint radius of the dispensed droplet, as illustrated in Figure 1c. Due to drop spreading, capillary imbibition, and evaporation, these parameters are time-dependent, which motivates the use of the maximum operators. In the case of line printing, the retardation factor R_f is analogously defined as

$$R_f \equiv \frac{\max(\Delta y_c) - \Delta y_0}{\max(\Delta y_w) - \Delta y_0} \tag{2}$$

where Δy_c and Δy_w represent the widths of the dye line and of the wet zone, respectively, as illustrated in Figure 1e. The deposition width Δy_0 of the printed line is the equivalent of the parameter $2R_0$ in the drop-casting experiments.

In this study, we deposited much higher ink volumes per unit area of paper than is customary in inkjet printing. When the deposited ink quantity exceeds the maximum holding capacity $\Theta_{tot,max} \approx 94$ g/m^2 of the paper substrate, the moisture content and the dye concentration will quickly equilibrate throughout the thickness direction of the paper sheet and subsequently spread along its lateral dimension in a quasi-1D fashion. This allows us to use microscopy as a non-destructive method for measuring the chromatographic separation of solvent and dye in a time-resolved fashion over large distances compared to the paper thickness. In commercial inkjet printing, the penetration depth of the colorant front is much smaller than the thickness of a paper sheet,[12] such that both lateral and vertical transport must be considered. However, the governing physical mechanisms are identical.

THEORETICAL MODEL

Murali *et al.* and Venditti *et al.* developed a theoretical model for the *in plane* transport of moisture, surface-active solutes, and heat in thin, fibrous, and moving porous media.[11,13] They assumed that at time t = 0, the transport and equilibration of moisture and colorant in the thickness direction were already complete. We adopted this model to describe the absorption and evaporation of an inkjet ink consisting of a non-surface-active colorant that is molecularly dissolved in a solvent after deposition onto a stationary horizontal sheet of paper. Below, we only list the main dynamic equations; for further details, the readers are referred to refs 11,13.

We use a Cartesian coordinate system with the x-axis parallel to the printing direction. The vertical z-axis is perpendicular to the horizontal paper sheet.

The model explicitly accounts for the presence of permeable fibers by means of a dual-porosity description. The moisture content Θ_f inside the fibers is assumed immobile.[14] Consequently, the dynamic equation for Θ_f (units kg/m^2) contains only flux terms but no transport terms

$$\frac{\partial \Theta_f}{\partial t} = s_{pf} - j_{ev,f} \tag{3}$$

https://doi.org/10.1021/acs.langmuir.1c01624
Langmuir 2021, 37, 11726−11736

Here, s_{pf} is the pore−fiber moisture exchange rate and $j_{ev,f}$ the evaporative flux from the fibers to the ambient atmosphere. The time evolution of the pore moisture content Θ_w is governed by the Richards equation,[15] integrated along the thickness direction of the paper substrate[11]

$$\frac{\partial \Theta_w}{\partial t} - \frac{\rho_w}{\mu_w}\nabla_{2D}(t_p K_w \nabla_{2D} p_w) = -j_{ev,w} - s_{pf} \tag{4}$$

where ρ_w and μ_w are the mass density and viscosity of the ink, respectively, t_p is the thickness of the paper, K_w is the permeability, p_w is the capillary pressure, $j_{ev,w}$ is the evaporative flux from the pores to the ambient atmosphere, and $\nabla_{2D} \equiv (\partial/\partial x, \partial/\partial y)$. We assume that K_w is unaffected by the presence of the colorant. Moreover, we assume that the ink viscosity increases with dye concentration according to the empirical relation

$$\mu(c) = \mu_{H_2O}\exp(c/c_1) \tag{5}$$

where $c_1 = 51.4$ kg/m^3. Equation 5 corresponds to the material properties of aqueous solutions of Triton X-100 and is chosen merely to illustrate the generic behavior.

The evaporation process is assumed to be diffusion-limited. The total evaporative flux j_{ev} is given by

$$j_{ev} \equiv j_{ev,w} + j_{ev,f} = k_\infty(\rho_v - \rho_{amb}) \tag{6}$$

where ρ_v is the water vapor concentration at the paper surface, ρ_{amb} is the ambient water vapor concentration, and k_∞ is a mass-transfer coefficient.

The total moisture content is defined as $\Theta_{tot} \equiv \Theta_w + \Theta_f$. Its value for paper in equilibrium with ambient conditions is denoted Θ_{amb}. In the following, we shall also be referring to the dimensionless total moisture content defined as $\theta_{tot} \equiv \Theta_{tot}/\Theta_s$, where $\Theta_s \approx 77$ g/m^2 is the mass density of a dry paper. The maximum water holding capacity of the paper substrate is denoted Θ_{max}. Its dimensionless variant is θ_{max}, which is assumed to have a value of[13] 1.5.

The heat transfer equation is given by[11]

$$(\rho c_p)_{av}\frac{\partial T}{\partial t} + \rho_w c_{p,w}\vec{v}_{2D}\cdot\nabla_{2D}T = = \frac{q_{2D}}{t_p} + \Phi_s + \nabla_{2D}\cdot(k_{av}\nabla_{2D}T) \tag{7}$$

where T is the temperature, $c_{p,w}$ the specific heat capacity of the ink, Φ_s is the heat of sorption, $\vec{v}_{2D} \equiv -(K_w/\mu_w)\nabla_{2D}p_w$ represents the in-plane components of the Darcy velocity, and k_{av} and $(\rho c_p)_{av}$ are the averaged thermal properties of wet paper. Moreover

$$q_{2D} \equiv h_\infty(T - T_{amb}) - j_{ev}E_{ev} \tag{8}$$

is the heat flux accounting for the heat exchange with the ambient environment and evaporative cooling. Here, $h_\infty = 9$ W/(m^{2}K) is the heat-transfer coefficient, T_{amb} is the ambient temperature, and $E_{ev} = 2.45$ MJ/kg is the enthalpy of evaporation of water. The transport of the colorant is governed by the following set of equations

$$\frac{\partial}{\partial t}(c\Theta_w) + \rho_w\nabla_{2D}\cdot(t_p c\vec{v}_{2D}) = = \nabla_{2D}\cdot[\Theta_w D_{2D}\nabla_{2D}c] - e_{pf} - s_{ad}\rho_w\Theta_s \tag{9}$$

$$\frac{\partial}{\partial t}(c_f\Theta_f) = e_{pf} \tag{10}$$

$$\frac{\partial C_{ad}}{\partial t} = s_{ad} \tag{11}$$

Here, c and c_f are the colorant concentrations (units kg of dye per cubic meter of ink) in the pores and fibers, respectively, and C_{ad} is the adsorbed colorant concentration (units kg of dye per kg of paper). The term $\Theta_w D_{2D}\nabla_{2D}c$ in eq 9 accounts for the diffusion and dispersion of the colorant. The dye in the fibers is assumed to be immobile. The term e_{pf} represents the pore−fiber exchange rate. There is no evaporative solute flux term because the colorant is assumed to be non-volatile. Evaporation-induced concentration increases are, however, accounted for, as a decrease in Θ_w automatically leads to a proportional increase in c. The right-hand side of eq 11 is the adsorptive flux

$$s_{ad} \equiv k_{ad}c\left[1 - \frac{C_{ad}}{C_\infty}\right] - k_{de}c_{ref}\frac{C_{ad}}{C_\infty} \tag{12}$$

which corresponds to the Langmuir adsorption isotherm[16] with adsorption and desorption rate constants k_{ad} and k_{de}, respectively, and sorption capacity C_∞. The parameter $c_{ref} = 0.15$ kg/m^3 is introduced merely such that k_{ad} and k_{de} have the same dimensions. The adsorption process described by eq 12 is completely reversible, that is, flushing with pure water will eventually desorb the colorant completely.

Boundary Conditions and Initial Conditions. We performed one- (1D) and two-dimensional (2D) numerical simulations using the computational domains in Figure 2a,b.

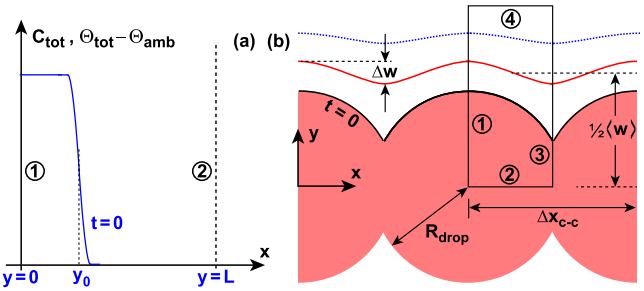

Figure 2. Sketch of the computational domains for the (a) 1D and (b) 2D simulations.

The corresponding initial conditions (ICs) are depicted as the blue curve in Figure 2a and the red distribution in Figure 2b. At time $t = 0$, we assume that imbibition of the ink in the thickness direction of the paper is already complete and that no ink is left on top of the paper. The water fronts and colorant fronts still coincide, that is, we assume that no adsorption has occurred, yet. Moreover, we assume that the water in the pores is in capillary equilibrium with the water in the fibers.

The blue curve in Figure 2a corresponds to the cross section of a printed line, as depicted in Figure 1e. The computational domain extends from the center of the printed line $y = 0$ to $y = L$, where L is chosen sufficiently large such that the water front never reaches the right boundary prior to complete evaporation. Consequently, the boundary conditions (BCs) at $y = 0$ correspond to mirror symmetry or no-flux conditions, that is, the y-derivatives of all quantities vanish there

https://doi.org/10.1021/acs.langmuir.1c01624
Langmuir 2021, 37, 11726−11736

$$\frac{\partial c}{\partial y} = 0 = \frac{\partial C_{ad}}{\partial y} = \frac{\partial \theta_w}{\partial y} = \frac{\partial \theta_f}{\partial y} = \frac{\partial T}{\partial y} \quad (13)$$

At the right boundary $y = L$, all quantities take their ambient values far away from the deposition zone, that is

$$c = 0 = c_f = C_{ad}, \qquad \theta_w = \theta_{w,amb}, \qquad T = T_{amb} \quad (14)$$

The 2D simulations consider the line formation in inkjet printing, that is, the deposition of a 1D array of individual droplets that will eventually merge. The individual droplets give rise to a periodic moisture distribution of period $\Delta x_{c-c} = 2\alpha R_{drop}$, where each period consists of a circular segment of radius R_{drop}. Typically, inkjet droplets are printed with a non-zero overlap, that is, the value of α is smaller than 1. Due to the inherent symmetries, the computational domain needs to span only half a period in the x-direction, as indicated by the black rectangle in Figure 2b. The corresponding BCs on the boundaries labeled ①, ②, and ③ correspond to no-flux conditions as

$$\vec{n}\cdot\nabla_{2D}c = 0 = \vec{n}\cdot\nabla_{2D}c_f = \vec{n}\cdot\nabla_{2D}\theta_w = \vec{n}\cdot\nabla_{2D}\theta_f \quad (15)$$

where $\vec{n}$ is a 2D unit normal vector defined at the boundaries of the computational domain. The height of the rectangle is sufficiently large such that the water front never reaches it. Consequently, the BCs on boundary ④ are given by eq 14. At $t = 0$, the positions of the water front and the colorant front are assumed to coincide [black solid line in Figure 2b].

Scales and Dimensionless Parameters. *Concentration.* The colorant concentration c of the ink is expressed in mass per unit volume of liquid (units kg/m^3). The sorption capacity C_∞ is usually given in mass of dye per unit mass of porous material (units mg/g). Consequently, a natural choice for a non-dimensionalized concentration is given by

$$\chi \equiv \frac{c\Theta_{tot}/\Theta_s}{\rho_w C_\infty} \quad (16)$$

where ρ_w is the solvent mass density.

Length- and Timescales. The relevant geometric lateral length scale is the half-width of the line y_0, which we assumed to be on the order of 1 mm. Moreover, several timescales can be devised

1. an evaporation timescale given by the quantity of water present initially divided by the evaporative flux $\tau_{evap} \equiv \theta_{tot}(y = 0, t = 0)/(k_\infty[\rho_s(t = 0) - \rho_{amb}])$, with typical value $\tau_{evap} \approx 10^3$ s.
2. an adsorption timescale $\tau_{ad} \equiv (k_{ad}c_0)^{-1}$, with typical value $\tau_{ad} \approx 10^3$ s.
3. a desorption timescale $\tau_{de} \equiv (k_{de}c_{ref})^{-1}$, with typical value $\tau_{de} \approx 10^5$ s.
4. a convective timescale $\tau_{flow} \equiv y_0/v_{Darcy}\ (t = 0)$, with typical value $\tau_{flow} \approx 10^2$ s.
5. a diffusive timescale $\tau_{diff} \equiv y_0^2/D_{2D}$, with typical value $\tau_{diff} \approx 10^4$ s.

There is also a thermal timescale associated with evaporative cooling and heat exchange with the ambient environment; however, in this paper, we do not focus on thermal effects. For the relatively large length scales considered, the diffusive timescale is typically longer than the others, which implies that diffusive effects are negligible. Since $\tau_{diff} \sim y_0^2$, this may not hold for smaller line widths.

One can also define an evaporation-induced length scale as $L_{evap} \equiv v_{Darcy}(t = 0)\tau_{evap}$, which is on the order of several centimeters and quantifies the maximum possible displacement of an imbibition front before complete evaporation.

RESULTS AND DISCUSSION

Experimental Results—Drop Casting. We performed drop-casting experiments using FSS and Rhodamine B solutions of different initial concentrations c_0, and the setup sketched in Figure 1a,b. Figure 1f shows the extracted retardation factor R_f as a function of c_0. The results qualitatively resemble those obtained by Koivunen *et al.* using the imbibition of tartrazine and safranine solutions from infinite reservoirs into porous layers that are comprised of calcium carbonate microparticles and polymeric binders.[17]

Experimental Results—Inkjet Deposition of Colorant Lines. We performed inkjet deposition experiments using FSS and Rhodamine B solutions, and the setup is sketched in Figure 1c. We varied the substrate speed and the droplet ejection frequency, as quantified by the mass deposition rate $\dot{m}$. Figure 3a–e shows top view photographs of inkjet-deposited lines of an FSS solution (c_0 = 0.025 wt %) for a substrate speed U_{IJ} = 0.2 mm/s and different values of $\dot{m}$. Figure 3f shows the transverse widths of the wet zone Δy_w and the dye line Δy_c as a function of $\dot{m}$. The solid lines correspond to power law relations $\Delta y_w \sim \dot{m}^{0.81}$, $\Delta y_{c,FSS} \sim \dot{m}^{0.59}$, and $\Delta y_{c,RB} \sim \dot{m}^{0.81}$, respectively, which represent the experimental data very well. The gray horizontal line corresponds to the approximate deposition width Δy_0. We estimated $\Delta y_0 \approx 0.2$ mm from a high-speed deposition experiment at U_{IJ} = 5 mm/s. For the two lowest values of $\dot{m}$, Δy_c remains close to Δy_0. This is due

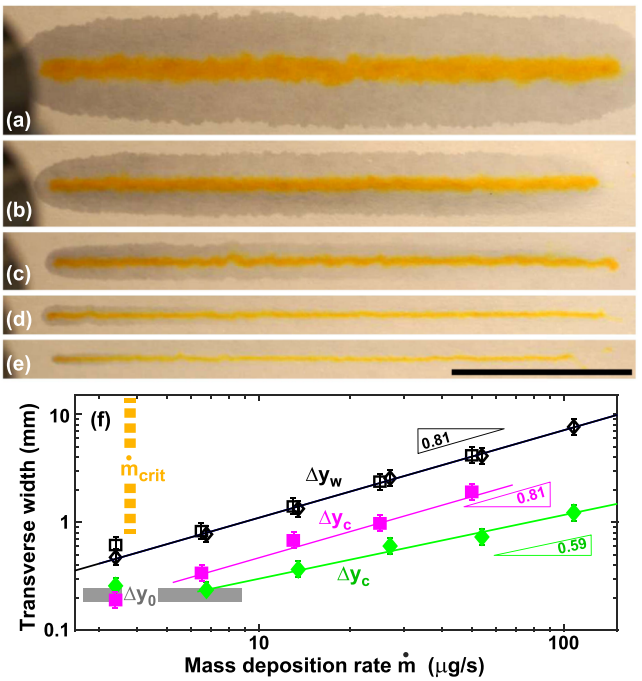

Figure 3. Top view photographs after inkjet deposition of lines of an FSS solution (c_0 = 0.025 wt %) for a substrate speed of U_{IJ} = 0.2 mm/s and different mass deposition rates $\dot{m}$ of (a) 108, (b) 54, (c) 27, (d) 13.5, and (e) 6.75 μg/s on Mondi DNS HSI NF paper. The scale bar in (e) represents 1 cm. (f) Transverse widths of the wet zone Δy_w (open symbols) and the dye line Δy_c (filled symbols) as a function of $\dot{m}$. Diamonds correspond to FSS (c_0 = 0.025 wt %) and squares to Rhodamine B (c_0 = 0.015 wt %).

https://doi.org/10.1021/acs.langmuir.1c01624
Langmuir 2021, 37, 11726−11736

to two reasons: for lower moisture contents, the permeability of the porous medium is much smaller, such that the moisture front progresses relatively less far before evaporation is complete. Moreover, in the limit of low ink mass deposition, the quantity of the colorant per unit mass of paper eventually falls below the effective dye sorption capacity.

Figure 4a–e shows top view photographs of inkjet deposited lines of an FSS solution (c_0 = 0.025 wt %) for a mass

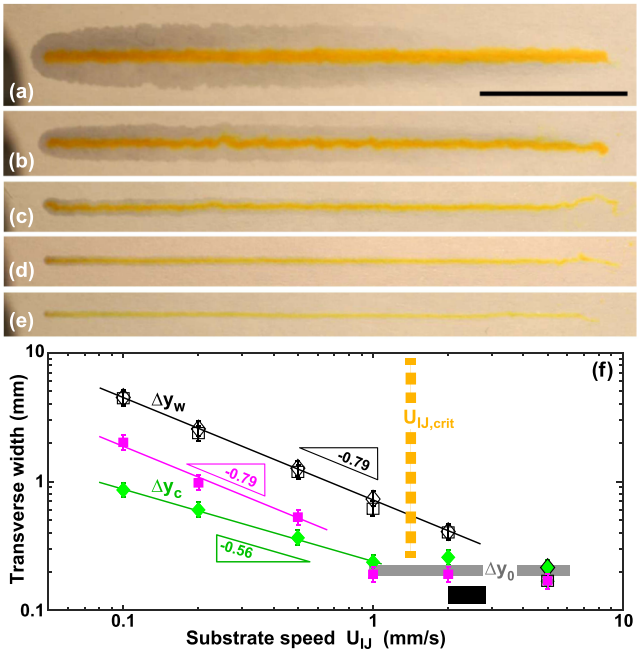

Figure 4. Top view photographs after inkjet deposition of lines of an FSS solution (c_0 = 0.025 wt %) for $\dot{m}$ = 27 μg/s and different substrate speeds U_{IJ} of (a) 0.1, (b) 0.2, (c) 0.5, (d) 1, and (e) 2 mm/s on Mondi DNS HSI NF paper. The scale bar in (a) represents 1 cm. (f) Transverse widths of the wet zone Δy_w (open symbols) and the dye line Δy_c (filled symbols) as a function of U_{IJ}. Diamonds correspond to FSS (c_0 = 0.025 wt %) and squares to Rhodamine B (c_0 = 0.015 wt %).

deposition rate of $\dot{m}$ = 27 μg/s and different values of the substrate speed U_{IJ}. Figure 4f shows Δy_w and Δy_c as functions of U_{IJ}. The solid lines correspond to power law relations $\Delta y_w \sim \dot{m}^{-0.79}$ and $\Delta y_{c,FSS} \sim \dot{m}^{-0.56}$ and $\Delta y_{c,RB} \sim \dot{m}^{-0.79}$, respectively, which represent the experimental data very well. The absolute values of the power law exponents are very close to the ones found in Figure 3f. This is because the mass of ink deposited per unit length of printed line is equal to $\dot{m}/U_{IJ}$. The power law exponents for Rhodamine B in both Figures 3f and 4f match those of the solvent front, whereas the absolute magnitude of those for FSS are smaller.

The data in Figures 3f and 4f imply that the retardation factor essentially approaches zero for small $\dot{m}$ and large U_{IJ} values. In the limits of large $\dot{m}$ or small U_{IJ} values, R_f approaches a constant value for Rhodamine B because the power law exponents of Δy_c and Δy_w are to good approximation identical. For FSS, the exponents are different, which implies that R_f will eventually approach zero for large $\dot{m}/U_{IJ}$. Consequently, from the perspective of preventing line broadening and maximizing resolution, printing at small values of $\dot{m}/U_{IJ}$ is preferable.

We expect a change in behavior when $\dot{m}/U_{IJ}$ falls below a critical value $\Theta_{tot,max}\Delta y_0$ determined by the maximum holding capacity of the paper and the deposition width. Below this value, the assumption of complete ink penetration in the thickness direction becomes unreliable. The vertical dashed lines in Figures 3f and 4f indicate the limiting values

$$\dot{m}_{crit} \equiv \Theta_{tot,\,max}\Delta y_0 U_{IJ}\,, \qquad U_{IJ,\,crit} \equiv \dot{m}/(\Theta_{tot,\,max}\Delta y_0) \tag{17}$$

for experiments performed with constant values of U_{IJ} and $\dot{m}$, respectively. The vertical dashed lines approximately coincide with the intersection of the power law fits for Δy_c with the constant levels Δy_0. Moreover, these limits coincide well with the visibility of the printed dye line on the backside of the paper sheet, that is, the occurrence of ink bleeding.

Numerical Results. In the following, we present systematic, 1D and 2D numerical simulations of colorant and moisture transport in a sheet of paper. In each plot, we focus on the effect of varying a single parameter (while keeping all others constant) on the chromatographic separation of the dye and the solvent. Unless specified otherwise, the values of the relevant parameters used in the simulations are those given in Table 1. Typical experimental values of the sorption capacity

Table 1. Parameter Values of the Base Case Considered in the Numerical Simulations

Parameter	value
k_{ad}	1×10^{-4} m^3/(kg s)
k_{de}	1×10^{-6} m^3/(kg s)
C_∞	1 mg/g
T_{amb}	298.15 K
k_∞	2.8×10^{-3} m/s
y_0	1 mm
$\theta_{tot}(y = 0, t = 0)$	0.98 θ_{max}

C_∞ for cellulosic materials range between 0.5 and 100 mg/g.[18−21] Typical experimental values of the dye adsorption timescale τ_{ad} for cellulosic materials range between 5 and 100 min.[20−24] The larger values are typically ascribed to diffusive intra-material transport processes before adsorption can take place.

Definition of Water and Colorant Front Positions. For the definition of the water and the colorant front positions, we need to define appropriate concentration thresholds. Since evaporation is taken into account in the model, the quantity of water in the paper will decrease as a function of time. Due to the ICs and inherent symmetries, the moisture distribution will always assume its maximum at y = 0. Therefore, if we defined a moisture content threshold relative to $\theta_{tot}(y = 0, t)$, the corresponding front position will at all times be on the order of y_0, irrespective of the evaporative moisture loss. Therefore, we define a threshold relative to the *initial* dimensionless total moisture content as 0.035 $[\theta_{tot}(y = 0, t = 0) - \theta_{amb}]$. This implies that the moisture front position y_w, defined as the maximum y-coordinate for which

$$\theta_{tot}(y, t) - \theta_{amb} > 0.035[\theta_{tot}(y = 0,\ t = 0) - \theta_{amb}] \tag{18}$$

holds, will start from y_0, first increase due to imbibition, reach a maximum, and eventually approach zero due to evaporation.

The colorant is assumed non-volatile. Consequently, the colorant concentration will tend to increase in time as the solvent evaporates. For this reason, we define the colorant threshold as 30% of the *current* maximum of the dye

https://doi.org/10.1021/acs.langmuir.1c01624
Langmuir 2021, 37, 11726−11736

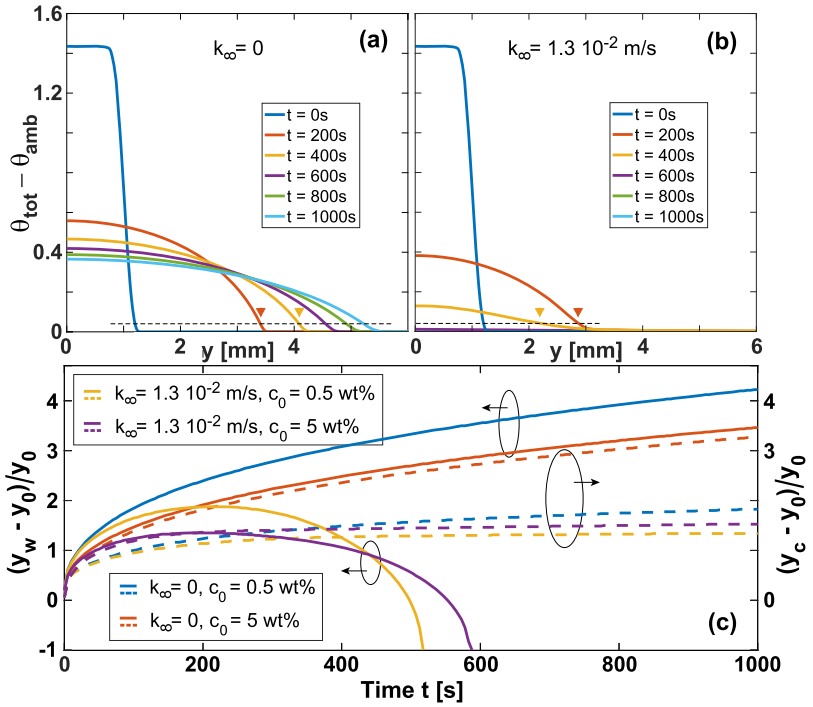

Figure 5. (a,b) Dimensionless total moisture content $\theta_{tot}(y) - \theta_{amb}$ for different times and (a) $k_\infty = 0$ (no evaporation) and (b) $k_\infty = 1.3 \times 10^{-2}$ m/s. The dashed horizontal lines indicate the threshold level defining the water front position. (c) Relative displacement of the moisture and colorant front positions $(y_w - y_0)/y_0$ (solid lines) and $(y_c - y_0)/y_0$ (dashed lines) as a function of time for different values of k_∞ and c_0.

concentration. Analogously, the colorant front position y_c is defined as the largest y-coordinate for which

$$C_{tot}(y,\ t) > 0.3 \max[C_{tot}(y,\ t)] \tag{19}$$

Here, the total mass of colorant per unit area of paper is defined as

$$C_{tot} \equiv \frac{c\Theta_w + c_f\Theta_f}{\rho_w} + C_{ad}\Theta_s \tag{20}$$

Figure 5a,b contrasts the dimensionless total moisture content profiles $\theta_{tot}(y) - \theta_{amb}$ for the cases of no evaporation ($k_\infty = 0$) and $k_\infty = 1.3 \times 10^{-2}$ m/s. Figure 5c shows typical examples of the time evolution of the water and the colorant front positions for different values of k_∞ and c_0.

The blue and orange sets of curves correspond to simulations for $k_\infty = 0$, that is, the absence of evaporation. The water and colorant fronts increase monotonically in time. The yellow and purple curves correspond to simulations for $k_\infty = 1.3 \times 10^{-2}$ m/s. In this case, the water front reaches a maximum extension before retracting. At $t \approx 550$ s, the curves terminate because the moisture content everywhere falls below the threshold value of $0.035\ \theta_{tot}(y = 0,\ t = 0)$. The colorant front position saturates roughly when y_w reaches its maximum.

As ICs, we used smoothed Heaviside functions for every variable, which drop from a constant value around $x = 0$ to the ambient value at a position $y = y_0$ [blue solid line in Figure 2a]. Thus, we can express the retardation factor as

$$R_f = \frac{\max(y_c) - y_0}{\max(y_w) - y_0} \tag{21}$$

Variation of Adsorption/Desorption Rates. In Figure 6a,b, we present the retardation factor R_f as a function of the initial concentration c_0 for different values of k_{ad} and k_{de}, as

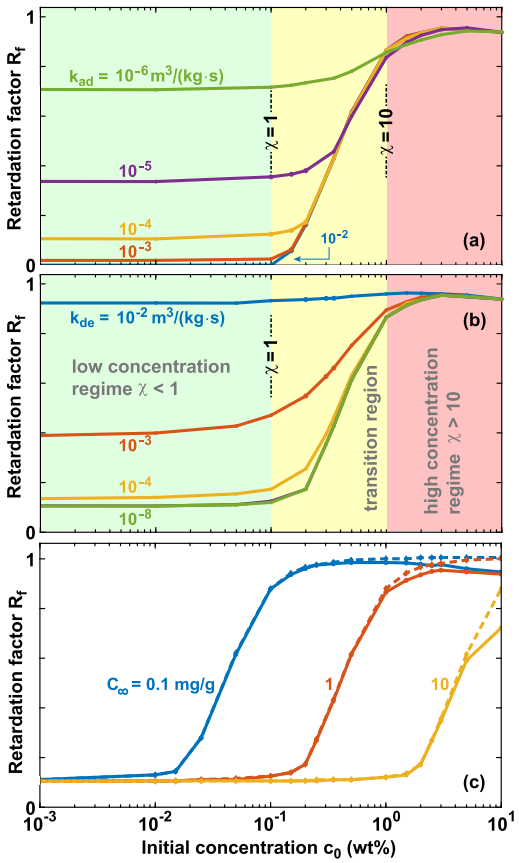

Figure 6. Retardation factor R_f as a function of the initial concentration c_0 as extracted from 1D simulations for different values of (a) the adsorption rate k_{ad}, (b) the desorption rate k_{de}, and (c) the sorption capacity C_∞.

https://doi.org/10.1021/acs.langmuir.1c01624
Langmuir 2021, 37, 11726−11736

extracted from 1D simulations. All curves exhibit a characteristic *S*-shape, that is, R_f is independent of c_0 for both low and high values of c_0 and exhibits a transition zone from a lower to a higher value of R_f that spans roughly 1 decade on the abscissa. The high-concentration value of R_f is generally close to 1 because the dye concentration eventually exceeds the sorption capacity of the paper. The low-concentration value of R_f strongly depends on the values of the adsorption rate k_{ad} and the desorption rate k_{de}. The transition zone is well described by the limits $1 \leq \chi_0 \equiv \chi(t = 0) \leq 10$.

An increase of k_{ad} reduces the low-concentration value of R_f because the dye is taken out of solution faster, which implies that it will be transported a shorter distance by the flow. An increase of k_{de} tends to increase the low-concentration value of R_f because the adsorbed colorant enters back into the mobile liquid phase faster. Conversely, the limit of $k_{de} \to 0$ (i.e., $\tau_{de} \to \infty$) implies that the colorant is irreversibly adsorbed, which reduces its transport distance and thus R_f. The adsorption and desorption rates are therefore an antagonistic pair of parameters as far as their effect on R_f is concerned.

We note that while R_f approaches 0 for sufficiently large k_{ad}, R_f may approach a non-zero value in the limit of small k_{de}, as observed in Figure 6b. This is because desorption is only relevant after adsorption has taken place and a relatively small value of k_{ad} (i.e., when $\tau_{ad} > \tau_{flow}$) can already enforce a finite value of $R_f > 0$.

Variation of the Sorption Capacity C_∞. The solid lines in Figure 6c illustrate the effect of varying the maximum sorption capacity C_∞ on the dependence of R_f on c_0. Primarily, an increase of C_∞ shifts the transition zone toward proportionally higher values of c_0. The dashed lines correspond to simulations assuming a concentration-independent ink viscosity $\mu(c) = \mu(c = 0)$. For initial concentrations $c_0 \geq 1$ wt % and large retardation factors, a small deviation is observed.

Variation of y_0 and the Initial Moisture Content. In the line deposition experiments described in the section Experimental Results—Inkjet Deposition of Colorant Lines, the variation of $\dot{m}$ and U_{IJ} effectively changes the width and the moisture content of the deposited line, which serves as the IC for the 1D simulations of the dye redistribution. Therefore, we varied the parameters y_0 (line half-width) and the initial dimensionless moisture content $\theta_{tot}(x = 0, t = 0)$ that characterize the IC [see Figure 2a]. Figure 7a,c illustrates the dependence of R_f on c_0 for different values of y_0 and $\theta_{tot}(x = 0, t = 0)$. In both cases, the highest sensitivity of R_f with respect to parameter variations is observed in the transition region. A higher moisture content leads to an increase of R_f over the entire range of initial concentrations. In contrast, a larger value of y_0 induces an increase of R_f in the transition region and a decrease in the low-concentration regime.

The solid lines in Figure 7b represent the relative increase of the half-width of the colorant line $\max(y_c) - y_0$ as a function of $\theta_{tot}(x = 0, t = 0)/\theta_{max}$ for different values of c_0. A higher moisture content always leads to a higher relative line broadening.

The solid lines in Figure 7d represent the increase of the half-width of the colorant line $\max(y_c) - y_0$ as a function of y_0 for different values of c_0. The dashed lines correspond to the maximum displacement of the moisture front $\max(y_w) - y_0$. In the limit of y_0 exceeding L_{evap}, all curves approach constant values, which implies that R_f no longer depends on y_0 for large y_0. For small $y_0 < 0.5$ mm, $\max(y_w) - y_0$ scales approximately as $y_0^{1/2}$, whereas the colorant front displacement scales linearly

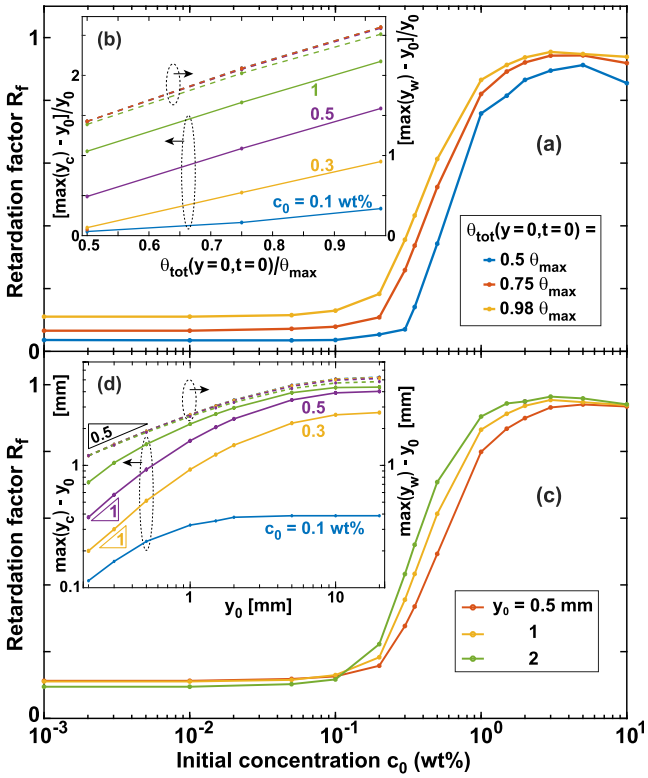

Figure 7. (a,c) Retardation factor R_f as a function of the initial concentration c_0 as extracted from 1D simulations for different values of (a) the dimensionless initial moisture content $\theta_{tot}(x = 0, t = 0)$ and (c) the initial line half-width y_0. (b,d) Maximum displacement of the colorant (solid lines) and moisture (dashed lines) front positions as a function of (b) $\theta_{tot}(x = 0, t = 0)/\theta_{max}$ and (d) y_0 for different values of c_0.

$\max(y_c) - y_0 \sim y_0$. For small $y_0 < 0.5$ mm, which is the regime relevant to the printing of text documents and line drawings, R_f thus increases with increasing y_0. The line width broadening is proportional to the line width, which implies that the *relative* line width broadening $[\max(y_c) - y_0]/y_0$ is constant in this regime. This makes it particularly easy to compensate for the broadening effects in the development of print strategies for a given combination of dye, solvent, and substrate.

Variation of the Evaporation Rate. In inkjet printing, the evaporation rate can be enhanced, for example, by measures that increase the mass-transfer coefficient k_∞—such as adding external convection in the gas phase—or by increasing the ambient temperature, which increases the solvent vapor pressure and thus the difference between ρ_s and ρ_{amb}. Evaporation has a strong effect on the time evolution of the water front position, as illustrated in Figure 5, and thus the time available for dye redistribution.

Figure 8a,c illustrates the effect of different mass-transfer coefficients k_∞ as well as different temperatures T_{amb} on the dependence of R_f on c_0. The retardation factor tends to increase with higher values of k_∞ and T_{amb}, except in the region where $R_f \geq 0.85$, where the curves essentially collapse. The biggest increment of R_f occurs in the transition region.

The solid lines in Figure 8b,d represent the relative increase of the normalized colorant line width $[\max(y_c) - y_0]/y_0$ as functions of k_∞ and T_{amb} for different values of c_0. The dashed lines in Figure 8b represent the maximum relative displacement of the water front $[\max(y_w) - y_0]/y_0$, which depends

https://doi.org/10.1021/acs.langmuir.1c01624
Langmuir 2021, 37, 11726−11736

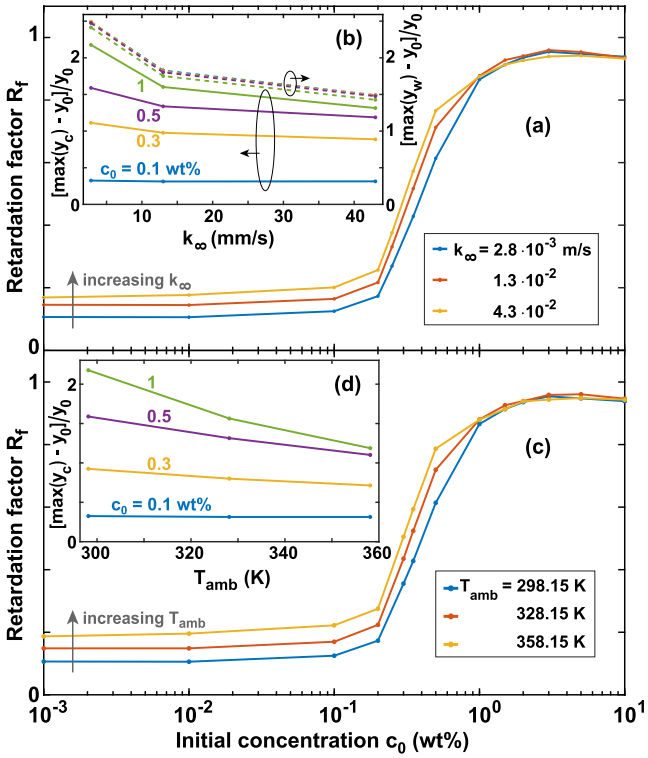

Figure 8. (a,c) Retardation factor R_f as a function of the initial concentration c_0, as extracted from 1D simulations for different values of (a) mass-transfer coefficient k_∞ and (c) ambient temperature T_{amb}. (b,d) Maximum relative displacement of the normalized colorant front position $[max(y_c) - y_0]/y_0$ (solid lines) as a function of k_∞ and T_{amb} for different values of c_0.

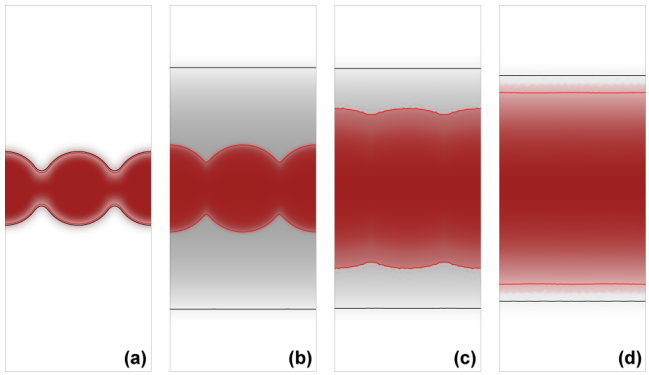

Figure 9. Pseudocolor plots of 2D simulations of the dye and moisture distributions for (R_{drop} = 200 μm and Δx_{c-c} = 400 μm) and different values of the initial concentration of (b) c_0 = 5 wt %, (c) 8 wt %, and (d) 10 wt %. (a) Initial condition t = 0 common to all cases. The black and red lines represent the solvent and colorant front positions. The shades of red and gray represent the total colorant per unit area of dry paper and total moisture concentrations c_{tot} and $\theta_{tot} - \theta_{amb}$, respectively. The red color scale in (b–d) is normalized to the maximum of C_{tot} defined in eq 20.

only weakly on c_0. The distance over which the water front spreads strongly depends on the effective evaporation rate. In contrast, the corresponding variation in $[\max(y_c) - y_0]/y_0$ is much weaker for initial concentrations c_0 below the transition region.

Line Formation in Dye-Based Inkjet Printing on Paper. In inkjet printing, individual droplets are deposited to generate arbitrary patterns. In the case of straight lines, it is usually desirable that the line width is as homogeneous as possible and does not exhibit undulations. If droplets are deposited with overlap, that is, with a center-to-center distance Δx_{c-c} smaller than the footprint diameter $2R_{drop}$ [for definitions, see Figure 2b], then undulations tend to be reduced. However, the minimum achievable line width then increases. This is the regime relevant to our inkjet deposition experiments in the Section Experimental Results—Inkjet Deposition of Colorant Lines.

Figure 9a illustrates the initial condition for an example of a 1D droplet array deposited with very small overlap, resulting in a large undulation amplitude at t = 0. Figure 9b–d compares the colorant and moisture distributions at t = 30 s for different values of c_0 corresponding to different values of the retardation factor R_f. For a small $R_f \leq 0.1$ [case (b)], the initial undulation amplitude remains essentially unchanged, while the solvent has spread to more than 3 times the initial line width $\langle w \rangle$ [for definitions, see Figure 2b]. For a medium $R_f \sim 0.5$ [case (c)], the undulation amplitude has decreased to about 50% of the initial value. For a large $R_f \geq 0.9$ [case (c)], the undulation is essentially gone completely, however, at the expense of a colorant line width $\langle w \rangle$ increasing to about 3 times its initial value.

Dye Precipitation. At first glance, it is surprising that the retardation factors for Rhodamine B and FSS in Figure 1f differ so strongly, although the molecular weights are comparable and both dyes have a xanthene core. The values of c_0, at which R_f reaches a level of 0.5, differ by approximately a factor of 10. We believe the origin of the difference to be due to the presence of divalent Ca^{2+} ions due to the $CaCl_2$ loading in the paper. Hou and Baughman and Vimonses *et al.* have studied the precipitation of anionic dyes in water containing Ca.[25,26] Analogous Ca-induced precipitation effects had previously been observed for anionic surfactants.[27−29]

Figure 10a–d presents the top view photographs after deposition of FSS solution droplets of different initial concentrations. The dashed circles approximately outline the maximum droplet footprint, as illustrated in Figure 1b. It is apparent that the color density and thus the dye concentration (per area of paper) have a local maximum at $r = R_0$ for all values of c_0. We interpret this as a consequence of a concentration maximum of Ca ions, which dissolve from the paper surface into the liquid droplet. Near the droplet contact line, the liquid thickness is the smallest. Thus, the ion concentration will be the highest (because the dilution of the Ca ion concentration will be the smallest) and FSS precipitation will primarily occur there. A second reason is that after a brief initial phase, after ink imbibition in the thickness direction is complete, there is flow inside the droplet toward the contact line because non-zero moisture content gradients in the paper then exist only beyond $r \geq R_0$. This phenomenon is akin to the evaporation-induced coffee-stain effect and transports the precipitated dye toward the contact line.

Figure 10e–h shows analogous images for Rhodamine-B solution droplets. The color density appears to be rather uniform for $r < R_{dye}$, that is, behind the dye front and no contact-line, enhancement of the dye concentration is observed. This points at the absence of $CaCl_2$-induced precipitation for the cationic dye.

https://doi.org/10.1021/acs.langmuir.1c01624
Langmuir 2021, 37, 11726−11736

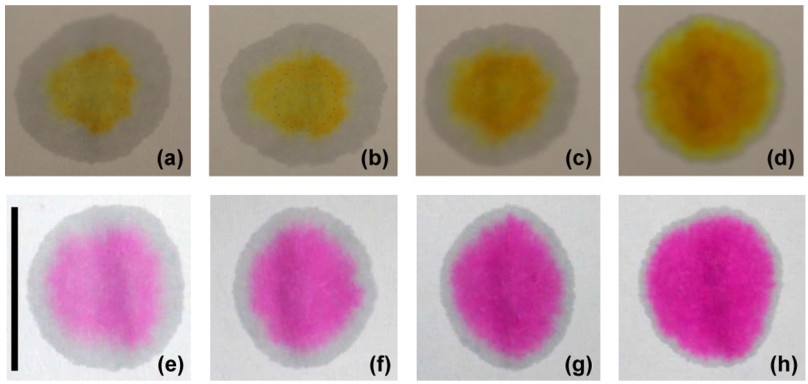

Figure 10. (a–d) Top view photographs after deposition of FSS solution droplets of initial concentrations: (a) 0.0125, (b) 0.025, (c) 0.05, and (d) 0.28 wt %. The dashed circles approximately outline the maximum droplet footprint, as illustrated in Figure 1b. (e–h) Analogous images after deposition of Rhodamine B solution droplets of initial concentrations: (a) 0.015, (b) 0.03, (c) 0.06, and (d) 0.12 wt %. The scale bar in (e) corresponds to 1 cm and is valid for all panels.

Technological Relevance. In principle, chromatographic effects are relevant to all printing processes. However, this is particularly true for inkjet printing because of the typically much lower solid content and much higher solvent concentration in inkjet inks that provide increased colorant mobility. A number of techniques have been developed in order to optimize the achievable resolution and pattern fidelity by improving and accelerating dye fixation. These include

(1) pretreatments by corona discharges and other plasmas,[30−36]
(2) the incorporation of ionic compounds into paper that have the opposite charge polarity as the dye,[7,37−40]
(3) the use of reactive dyes that form covalent bonds,[41−43]
(4) the use of nanoporous coating layers that increase the effective surface area,[7]
(5) the use of binders that reduce the permeability and thus the ink absorption rate,[7] or
(6) an increase of the solvent evaporation rate by increasing the temperature or by using microwave or infrared irradiation to reduce the time available for ink transport.[44−49]

In the framework of our adsorption model, strategies 1 to 4 aim at an increase of c_∞ and k_{ad} and/or a decrease of k_{de}, all of which tend to reduce R_f. Strategies 5 and 6 directly aim at minimizing solvent transport.

Our results are not only relevant to dye-based printing inks but also to pigment-based inks because the latter typically contain a number of molecularly dissolved additives that are subject to the same retardation phenomena as the dyes we investigated.

CONCLUSIONS

We have studied the transport and chromatographic separation of a model ink consisting of a dilute solution of a colorant in a solvent in thin porous media. We conducted systematic experiments using drop-casting and inkjet deposition of solutions of an anionic and a cationic dye in water on a commercial paper type. The paper was loaded with $CaCl_2$ in order to facilitate colorant fixation. This leads to a precipitation reaction of the anionic colorant on top of and inside the paper, while the cationic dye was apparently unaffected. The chromatographic retardation as a function of initial concentration of the two dyes differed by an order of magnitude despite their similar molecular weights and although both have a xanthene core.

We developed a comprehensive numerical model that accounts for unsaturated flow and chromatographic separation of a dye solution as well as the presence of permeable fibers, solvent evaporation, and heat-transfer effects. The model qualitatively reproduces the dependence of the retardation factor on the dye concentration. We have systematically varied the key parameters and evaluated their effect on the broadening and width fluctuations of inkjet-deposited colorant lines.

The sensitivity of the retardation factor R_f to changes in operating conditions is generally the highest in the transition region, which spans roughly a decade in dye concentration in our model and where R_f changes from a low-concentration to a high-concentration value. In order to optimize pattern fidelity, printing should be performed with the smallest moisture content, the highest adsorption and the lowest desorption rates, the highest evaporation rate, and the lowest dye concentration possible. In contrast, the reproduction of strong, saturated colors, however, requires a minimum colorant concentration depending on the paper type.

AUTHOR INFORMATION

Corresponding Author

Anton A. Darhuber − *Department of Applied Physics, Eindhoven University of Technology, Eindhoven 5600MB, The Netherlands;* orcid.org/0000-0001-8846-5555; Email: a.a.darhuber@tue.nl

Authors

Gianmarco Venditti − *Department of Applied Physics, Eindhoven University of Technology, Eindhoven 5600MB, The Netherlands*

Vignesh Murali − *Department of Applied Physics, Eindhoven University of Technology, Eindhoven 5600MB, The Netherlands*

Complete contact information is available at: https://pubs.acs.org/10.1021/acs.langmuir.1c01624

Author Contributions

V.M. developed the experimental setup and the measurement protocols. He conducted all the experiments and analyzed the experimental data. The theoretical model was jointly

https://doi.org/10.1021/acs.langmuir.1c01624
Langmuir 2021, 37, 11726−11736

developed by G.V. and A.D. G.V. performed all the numerical simulations and analyzed the numerical data. The manuscript was written by V.M., G.V., and A.D. The research was conceived and guided by A.D.

Notes

The authors declare no competing financial interest.

■ ACKNOWLEDGMENTS

This work was part of the research programme "The role of surfactants in spreading, imbibition and sorption of water-based printing inks" with project number 14666, which was (partly) financed by the Netherlands Organisation for Scientific Research (NWO). The authors thank Nicolae Tomozeiu, Herman Wijshoff, and Louis Saes of Canon Production Printing for their valuable cooperation.

■ REFERENCES

(1) Snyder, L. R.; Kirkland, J. J.; Dolan, J. W. *Introduction to Modern Liquid Chromatography*; 3rd ed; John Wiley & Sons, 2010.
(2) Kuhn, A. O.; Lederer, M. Adsorption chromatography on cellulose: II. Separations of aromatic amino acids, biogenic amines, alkaloids, dyes and phenols and determination of hydrophobic constants. *J. Chromatogr. A* **1988**, *440*, 165−182.
(3) Spangenberg, B.; Poole, C. F.; Weins, C. *Quantitative Thin-Layer Chromatography*; Springer-Verlag, 2011.
(4) Yu, W. W.; White, I. M. Chromatographic separation and detection of target analytes from complex samples using inkjet printed SERS substrates. *Analyst* **2013**, *138*, 3679−3686.
(5) Abbas, A.; Brimer, A.; Slocik, J. M.; Tian, L.; Naik, R. R.; Singamaneni, S. Multifunctional Analytical Platform on a Paper Strip: Separation, Preconcentration, and Subattomolar Detection. *Anal. Chem.* **2013**, *85*, 3977−3983.
(6) Magdassi, S. *The Chemistry of Inkjet Inks*; World Scientific, 2009.
(7) Donigian, D.; Wernett, P. C.; McFadden, M.; McKay, J. J. Ink-jet dye fixation and coating pigments. *Tappi J.* **1999**, *82*, 175−182.
(8) Sodhi, R. N. S.; Sun, L.; Sain, M.; Farnood, R. Analysis of Ink/Coating Penetration on Paper Surfaces by Time-of-Flight Secondary Ion Mass Spectrometry (ToF-SIMS) in Conjunction with Principal Component Analysis (PCA). *J. Adhes.* **2008**, *84*, 277−292.
(9) Filenkova, A.; Acosta, E.; Brodersen, P. M.; Sodhi, R. N. S.; Farnood, R. Distribution of inkjet ink components via ToF-SIMS imaging. *Surf. Interface Anal.* **2011**, *43*, 576−581.
(10) Lamminmäki, T. T.; Kettle, J. P.; Puukko, P. J. T.; Gane, P. A. C. The chromatographic separation of anionic dye in inkjet coating structures. *Colloids Surf., A* **2011**, *377*, 304−311.
(11) Murali, V.; Venditti, G.; Zeegers, J. C. H.; Darhuber, A. A. Inkjet deposition of lines onto thin moving porous media - experiments and simulations. *Int. J. Heat Mass Transfer* **2021**, *176*, 121466.
(12) Desie, G.; Van Roost, C. Validation of Ink Media Interaction Mechanisms for Dye and Pigment-based Aqueous and Solvent Inks. *J. Imaging Sci. Technol.* **2006**, *50*, 294−303.
(13) Venditti, G.; Murali, V.; Darhuber, A. A. Inkjet deposition of surfactant solutions onto thin moving porous media - experiments and simulations, **2021**, submitted.
(14) Marin Zapata, P. A.; Fransen, M.; ten Thije Boonkkamp, J.; Saes, L. Coupled heat and moisture transport in paper with application to a warm print surface. *Appl. Math. Model.* **2013**, *37*, 7273−7286.
(15) Szymkiewicz, A. *Modelling water flow in unsaturated porous media: accounting for nonlinear permeability and material heterogeneity*; Springer: New York, 2013.
(16) Langmuir, I. The Adsorption of Gases on Plane Surfaces of Glass, Mica and Platinum. *J. Am. Chem. Soc.* **1918**, *40*, 1361−1403.
(17) Koivunen, R.; Jutila, E.; Bollström, R.; Gane, P. Investigating chromatographic interactions in porous pigment coatings between inkjettable polyelectrolytes and model colorant solutions. *Colloids Surf., A* **2019**, *579*, 123676.
(18) Široký, J.; Blackburn, R. S.; Bechtold, T.; Taylor, J.; White, P. Alkali treatment of cellulose II fibres and effect on dye sorption. *Carbohydr. Polym.* **2011**, *84*, 299−307.
(19) Arami, M.; Limaee, N.; Mahmoodi, N.; Tabrizi, N. Equilibrium and kinetics studies for the adsorption of direct and acid dyes from aqueous solution by soy meal hull. *J. Hazard. Mater.* **2006**, *135*, 171−179.
(20) Halysh, V.; Sevastyanova, O.; Pikus, S.; Dobele, G.; Pasalskiy, B.; Gun'ko, V. M.; Kartel, M. Sugarcane bagasse and straw as low-cost lignocellulosic sorbents for the removal of dyes and metal ions from water. *Cellulose* **2020**, *27*, 8181−8197.
(21) Lafi, R.; Abdellaoui, L.; Montasser, I.; Hafiane, A. Removal of methyl orange from aqueous solution onto modified extracted cellulose from Stipa Tenacissima L. *Int. J. Environ. Anal. Chem.* **2020**, 1−17.
(22) Zhou, C.-H.; Zhang, D.; Tong, D.-S.; Wu, L.-M.; Yu, W.-H.; Ismadji, S. Paper-like composites of cellulose acetate−organo-montmorillonite for removal of hazardous anionic dye in water. *Chem. Eng. J.* **2012**, *209*, 223−234.
(23) Roy, A.; Adhikari, B.; Majumder, S. B. Equilibrium, Kinetic, and Thermodynamic Studies of Azo Dye Adsorption from Aqueous Solution by Chemically Modified Lignocellulosic Jute Fiber. *Ind. Eng. Chem. Res.* **2013**, *52*, 6502−6512.
(24) Laureano-Anzaldo, C. M.; Haro-Mares, N. B.; Meza-Contreras, J. C.; Robledo-Ortíz, J. R.; Manríquez-González, R. Chemical modification of cellulose with zwitterion moieties used in the uptake of red Congo dye from aqueous media. *Cellulose* **2019**, *26*, 9207−9227.
(25) Hou, M.; Baughman, G. L. Predicting the precipitation of acid and direct dyes in natural waters. *Dyes Pigm.* **1992**, *18*, 35−46.
(26) Vimonses, V.; Jin, B.; Chow, C. W. K. Insight into removal kinetic and mechanisms of anionic dye by calcined clay materials and lime. *J. Hazard. Mater.* **2010**, *177*, 420−427.
(27) Watanabe, A. Physico-chemical Studies on Surface Active Agents. (V) The Precipitation of Anionic Surface Active Agents by Metal Ions. *Bull. Inst. Chem. Res. Kyoto Univ.* **1960**, *38*, 248−273.
(28) Peacock, J. M.; Matijević, E. Precipitation of alkylbenzene sulfonates with metal ions. *J. Colloid Interface Sci.* **1980**, *77*, 548−554.
(29) Stellner, K. L.; Scamehorn, J. F. Hardness tolerance of anionic surfactant solutions. 1. Anionic surfactant with added monovalent electrolyte. *Langmuir* **1989**, *5*, 70−77.
(30) Carlsson, C. M. G.; Stroem, G. Reduction and oxidation of cellulose surfaces by means of cold plasma. *Langmuir* **1991**, *7*, 2492−2497.
(31) Fang, K.; Wang, S.; Wang, C.; Tian, A. Inkjet printing effects of pigment inks on silk fabrics surface-modified with O2 plasma. *J. Appl. Polym. Sci.* **2008**, *107*, 2949−2955.
(32) Tuominen, M.; Lahti, J.; Lavonen, J.; Penttinen, T.; Räsänen, J. P.; Kuusipalo, J. The Influence of Flame, Corona and Atmospheric Plasma Treatments on Surface Properties and Digital Print Quality of Extrusion Coated Paper. *J. Adhes. Sci. Technol.* **2010**, *24*, 471−492.
(33) Ovaska, S.-S.; Mielonen, K.; Backfolk, K.; Lozovski, T.; Rinkunas, R.; Sidaravicius, J. A novel approach for studying the effects of corona treatment on ink-substrate interactions. *Nord. Pulp Pap. Res. J.* **2015**, *30*, 681−688.
(34) Pawlat, J.; Terebun, P.; Kwiatkowski, M.; Diatczyk, J. RF atmospheric plasma jet surface treatment of paper. *J. Phys. D: Appl. Phys.* **2016**, *49*, 374001.
(35) Zhang, C.; Wang, L.; Yu, M.; Qu, L.; Men, Y.; Zhang, X. Surface processing and ageing behavior of silk fabrics treated with atmospheric-pressure plasma for pigment-based ink-jet printing. *Appl. Surf. Sci.* **2018**, *434*, 198−203.
(36) Navik, R.; Shafi, S.; Alam, M. M.; Farooq, M. A.; Lin, L.; Cai, Y. Influence of dielectric barrier discharge treatment on mechanical and dyeing properties of wool. *Plasma Sci. Technol.* **2018**, *20*, 065504.

https://doi.org/10.1021/acs.langmuir.1c01624
Langmuir 2021, 37, 11726−11736

(37) Yu, P.-C.; Chen, C.-I.; Yang, R.-J.; Yen, F.-S.; Max Yen, S.-T. Porous χ-Al_2O_3 Flake Powder as Dye-Fixing Materials for Inkjet Printing Paper. *J. Am. Ceram. Soc.* **2012**, *95*, 2124−2126.
(38) Mielonen, K.; Geydt, P.; Österberg, M.; Johansson, L.-S.; Backfolk, K. Inkjet ink spreading on polyelectrolyte multilayers deposited on pigment coated paper. *J. Colloid Interface Sci.* **2015**, *438*, 179−190.
(39) Mielonen, K.; Laukala, T.; Lyytikäinen, J.; Backfolk, K. The effect of anionic-cationic multilayering and microstructure on dye-based ink absorption. *Chem. Eng. Sci.* **2018**, *190*, 396−404.
(40) Yang, H.; Fang, K.; Liu, X.; An, F. High-Quality Images Inkjetted on Different Woven Cotton Fabrics Cationized with P(St-BA-VBT) Copolymer Nanospheres. *ACS Appl. Mater. Interfaces* **2019**, *11*, 29218−29230.
(41) Lewis, D.. In *Handbook of Textile and Industrial Dyeing*; Clark, M., Ed.; Woodhead Publishing Series in Textiles; Woodhead Publishing, 2011; Vol. *1*, pp 303−364.
(42) Li, M.; Zhang, L.; An, Y.; Ma, W.; Fu, S. Relationship between silk fabric pretreatment, droplet spreading, and ink-jet printing accuracy of reactive dye inks. *J. Appl. Polym. Sci.* **2018**, *135*, 46703.
(43) Song, Y.; Fang, K.; Bukhari, M. N.; Ren, Y.; Zhang, K.; Tang, Z. Green and Efficient Inkjet Printing of Cotton Fabrics Using Reactive Dye@Copolymer Nanospheres. *ACS Appl. Mater. Interfaces* **2020**, *12*, 45281−45295.
(44) Eastlund, B. J.; Spann, D. E.; Alfekri, D. M. Microwave energy ink drying method. US Patent 6(508), 550 B12003.
(45) Seccombe, S. D. Printer including microwave dryer. US Patent 6,578,959 B12003.
(46) Wotton, G.; Klopfenstein, M. Microwave applicator for inkjet printer. US Patent 6,663,239 B22003.
(47) Wolnick, K.; Decker, W. Infrared dryer for printing presses. US Patent 4,809,608, 1989.
(48) Li, Y.; Gu, W. J.; He, B. G. Research on the Influence of Drying Method on Ink Penetration of Coated Paper. *Adv. Mater. Res.* **2014**, *884−885*, 312−315.
(49) Jingxiang, X.; Jinyao, L.; Haichao, L.; Mingming, Z.; Jifei, C. Research Progress on Water-based Ink Drying Technology. *IOP Conf. Ser.: Mater. Sci. Eng.* **2019**, *565*, 012017.

https://doi.org/10.1021/acs.langmuir.1c01624
Langmuir 2021, 37, 11726−11736